Microwave spectra of dinitrotoluene isomers: a new step towards the detection of explosive vapors

Mhamad Chrayteh, Pascal Dréan, Manuel Goubet, Laurent H. Coudert, Anthony Roucou, Arnaud Cuisset

▶ **To cite this version:**

Mhamad Chrayteh, Pascal Dréan, Manuel Goubet, Laurent H. Coudert, Anthony Roucou, et al.. Microwave spectra of dinitrotoluene isomers: a new step towards the detection of explosive vapors. Physical Chemistry Chemical Physics, 2023, 25 (24), pp.16307-16318. 10.1039/d3cp01577g . hal-04172070

HAL Id: hal-04172070
https://hal.science/hal-04172070

Submitted on 27 Jul 2023

HAL is a multi-disciplinary open access archive for the deposit and dissemination of scientific research documents, whether they are published or not. The documents may come from teaching and research institutions in France or abroad, or from public or private research centers.

L'archive ouverte pluridisciplinaire **HAL**, est destinée au dépôt et à la diffusion de documents scientifiques de niveau recherche, publiés ou non, émanant des établissements d'enseignement et de recherche français ou étrangers, des laboratoires publics ou privés.

PCCP

ARTICLE TYPE

Cite this: DOI: 00.0000/xxxxxxxxxx

Microwave spectra of dinitrotoluene isomers: a new step towards the detection of explosive vapors †

Mhamad Chrayteh,*[a] Pascal Dréan,[b] Manuel Goubet,[b] Laurent H. Coudert,[c] Anthony Roucou,[a] and Arnaud Cuisset*[a]

Received Date
Accepted Date

DOI: 00.0000/xxxxxxxxxx

The spectroscopic characterization of explosives taggants used for TNT detection is a research topic of growing interest. We present a gas-phase rotational spectroscopic study of weakly volatile dinitrotoluenes (DNT) isomers. The pure rotational spectra of 2,4-DNT and 2,6-DNT were recorded in the microwave range (2–20 GHz) using a Fabry-Perot Fourier-transform microwave (FP-FTMW) spectrometer coupled to a pulsed supersonic jet. Rotational transitions are split by hyperfine quadrupole coupling at the two ^{14}N nuclei leading to up to 9 hyperfine components. The spectral analysis was supported by quantum chemical calculations carried out at the B98/cc-pVTZ and MP2/cc-pVTZ levels of theory. The methyl group internal rotation barriers were calculated to be $V_3 = 515\,\mathrm{cm}^{-1}$ and $698\,\mathrm{cm}^{-1}$ for respectively 2,4- and 2,6-DNT. Although no splitting due to internal rotation was observed for 2,6-DNT, several splittings were observed for 2,4-DNT. The microwave spectrum of both species were fitted using a semi-rigid Hamiltonian accounting for the quadrupole coupling hyperfine structure. Based on the internal axis method (IAM), an additional analysis was performed to retrieve an accurate value of the rotationless A-E tunneling splitting which could be extracted from the rotational dependence of the tunneling splitting. This yielded in the case of 2,4-DNT to an experimental value of $525\,\mathrm{cm}^{-1}$ for the barrier height V_3 which agrees well with the DFT value. The coupled internal rotations of $-CH_3$ and $-NO_2$ is investigated in terms of 2-D surfaces, as already done in the case of 2-nitrotoluene [Roucou *et al., Chem. Phys. Chem.,* 2020, **21,** 2523–2538].

1 Introduction

The detection and characterization of explosives, of their taggants, or of their degradation products is a topic of crucial importance for public safety. It undoubtedly plays a key role in airports protection against terrorist attacks. It is also important for luggage screening and bombing scene investigations. With a sample of the explosive or of the post-blast debris, analytical tools like liquid or gas chromatography coupled to mass spectrometry or vacuum ultraviolet spectroscopy can be used [1,2] for chemical analysis. Laser induced photoacoustic spectroscopy can be optimized in order to identify trace compounds of explosive materials deposited on surfaces. [3] Low resolution absorption terahertz (THz) spectroscopy is also a technique that can be used to identify explosives in condensed phase that possess specific spectral signatures in this spectral domain. [4] It was successfully applied to the detection of ammonium nitrate, 2,4,6-trinitrotoluene (TNT) and its degradation product 2,4-dinitrotoluene, 1,3,5,7-tetranitro-1,3,5,7-tetrazocane (HMX), cyclo-1,3,5-trimethylene-2,4,6-trinitramine (also known as cyclonite, hexogen, T4, or RDX), 1,3-dinitrato-2,2-bis(nitratomethyl)-propane (PETN), and 2,3-dimethyl-2,3-dinitrobutane (DMNB). [5]

Unlike the techniques outlined in the previous paragraph, used for chemical analysis, there also exist many techniques developed for detection of gas phase explosives or their related compounds. They aim at overcoming the very low vapor pressure of these species at room temperature. One of the most powerful method is ion mobility spectrometry. [6–8] It consists in ionizing (using X-ray, laser or high voltage discharge) a gaseous sample of contaminated air collected near a source, for instance a luggage containing explosives. The ionized molecules are then separated by their mobility difference when subject to the electric field. High-resolution spectroscopic techniques also turn out to be very effective for gas phase explosive detection, the reader is

[a] Université du Littoral Côte d'Opale, UR 4493, Laboratoire de Physico-Chimie de l'Atmosphère, F-59140 Dunkerque, France. E-mail: mhamad.chrayteh@univ-littoral.fr; arnaud.cuisset@univ-littoral.fr

[b] Univ. Lille, CNRS, UMR8523 - PhLAM - Physique des Lasers Atomes et Molécules, F-59000 Lille, France

[c] Université Paris-Saclay, CNRS, Institut des Sciences Moléculaires d'Orsay, 91405 Orsay, France

† Electronic Supplementary Information (ESI) available: [details of any supplementary information available should be included here]. See DOI: 10.1039/cXCP00000x/

referred to Ref. 9 for a review. At least two challenges need to be addressed: the detection limit should be better than 1 ppb and the discriminating power should allow to unambiguously identify chemical species despite of similar properties. Such a high sensitivity is required due to the very low vapor pressure that classical explosives such as cyclo-1,3,5-trimethylene-2,4,6-trinitramine or the nitroaromatic explosive trinitrotoluene (TNT) exhibit at room temperature (e.g. $\approx 2.7 \times 10^{-4}$ mbar for TNT).[10] Alternatively, spectroscopic techniques can be applied to the detection of explosive taggants which are intentionally added to explosives or found as impurities due to the manufacturing process or the degradation. For instance, a sample of TNT contains mononitroluenes (NT) and dinitrotoluenes (DNT) that are more volatile than TNT and can be targeted to detect this species. For this purpose, Two types of spectroscopic techniques are available. Laser-based techniques have been widely used and rely on the extensive results available about nitroaromatics. In 2006, Pushkarsky *et al.*[10] claimed that they could detect TNT at levels as low as 0.1 ppb using quantum cascade laser-based photoacoustic spectroscopy around 7.3 μm. However, unknown impurities absorbing in the same wavelength region may skew the detection results. In 2010, Snels *et al.*[11] recorded the gas phase spectra of 2,4-DNT, 2,6-DNT, and TNT using a cw cavity ringdown spectrometer operating in the 1560–1680 nm wavelengths range and heating the compounds at 150 °C. Absorption peaks with an full width at half maximum (FWHM) close to 15 nm were observed for each species at 1644, 1562 and 1640 nm. Although the resolution of the technique allowed the three compounds to be discriminated, its sensitivity was too low to detect them at room temperature.

High resolution rotational and rovibrational spectroscopy, from the microwave to the THz domains, is a powerful technique able to discriminate molecular polar compounds with very close geometries such as isotopologues,[12] isomers,[13] and conformers.[14,15] With such a technique, the gas phase monitoring of volatile or semi-volatile organic compounds at trace levels becomes feasible in realistic environments of complex chemical mixtures. Recently, the rotational spectra of the meta-, ortho-, and para-nitrotoluenes were investigated[13,16] using millimeter wave spectroscopy. Line splittings due to the methyl group internal rotation were observed for the three isomers. Additional splittings attributed to the nitro group internal rotation were also observed for some transitions. Fewer results are available about larger nitroaromatics such as 2,4-DNT and 2,6-DNT. Foltynowicz *et al.*[17] reported the first known gas phase rotational spectrum of 2,4-DNT measured at room temperature by THz time domain spectroscopy. Unfortunately, resolution and sensitivity were insufficient to produce the necessary rotational linelist required for an unambiguous monitoring of the TNT taggant.

The microwave spectra of these two species were recorded with an Fabry-Perot Fourier Transform MicroWave (FP-FTMW) spectrometer coupled to a pulsed supersonic jet and line frequency analyses were carried out. The spectroscopic parameters thus determined include the rotational and distortion constants as well as effective nuclear quadrupole coupling constants describing the hyperfine splittings arising from the two ^{14}N nuclei. In the case of 2,4-DNT, small torsional splittings were also observed and accounted for using an effective approach allowing us to determine V_3 , the height of the three fold potential barrier hindering the methyl group internal rotation. In order to confirm the assignment of the rotational spectra in terms of isomeric species, the rotational and centrifugal distortion spectroscopic parameters were compared with their theoretical values using calculations carried out in this work at the B98/cc-pVTZ and MP2/cc-pVTZ levels of theory. A qualitative explanation of the changes in the V_3 value when going from 2-NT to 2,4-DNT and 2,6-DNT is provided utilizing their molecular electrostatic potential. Finally, a numerical determination of V_3 is performed for the two latter species based on their potential energy surface computed using quantum chemical calculations and parameterized in terms of the methyl and nitro groups dihedral angles.

2 Theory

2.1 Optimized geometries and potential energy functions

Quantum chemical calculations were performed in this investigation using the Gaussian 16 rev. B.01 software[18] implemented in the High-Performance Computing Linux cluster of the PhLAM laboratory. Geometry optimization of both DNT isomers were carried out using the Møller-Plesset perturbation theory to second order (MP2)[19] and density functional theory (B98)[20] combined with triple-correlation-consistent polarized valence basis sets (cc-pVTZ).[21] The tight convergence option was utilized. The optimized geometries of 2,4-DNT and 2,6-DNT are respectively shown in Figs. 1 and 2. The quartic centrifugal distortion constants in the harmonic approximation were estimated for these optimized geometry.

The torsional energy functions of 2,4-DNT and 2,6-DNT are investigated at the B98/cc-pVTZ level of theory in Section 4.3. For the simpler case of 2,4-DNT, a potential energy function was computed as a function of the dihedral angle $\alpha = \angle C_2C_1C_7H_4$ which, as emphasized in Fig. 1, parameterizes the internal rotation of the methyl group. The potential energy function retrieved displays three-fold symmetry and three equivalent minima at α=0, 120, and 240°. The height of the torsional barrier between each minimum V_3 was calculated to be 515 cm^{-1} in Section 4.3.1.

As stressed in Section 4.3, treating the more complicated case of 2,6-DNT requires allowing for the fact that both $-NO_2$ groups can also undergo internal rotation; the value retrieved by Larsen[22] for the two fold barrier hindering the internal rotation of the single nitro group in nitrobenzene is only 1570(170) cm^{-1}. The strong coupling between the $-NO_2$ and $-CH_3$ groups should also be taken into account. It can be understood qualitatively in terms of steric hindrance as the two $-NO_2$ moieties, on both sides of the methyl group, are in close proximity to that group. A detailed numerical evaluation of the 2,6-DNT torsional barrier, taking into account the strong coupling between nitro and methyl groups, is presented in Section 4.3.2.

In order to understand qualitatively how steric hindrance effects alter the potential energy surface (PES) of 2,6-DNT, a 2-D potential energy surface was computed using chemical intuition and symmetry considerations. This surface is computed in the weak and strong steric hindrance limiting cases and parameter-

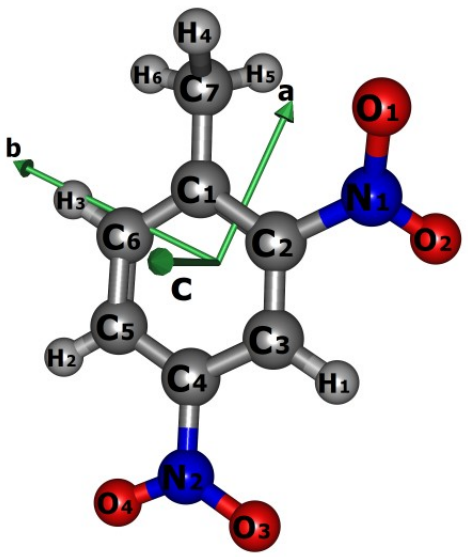

(a)

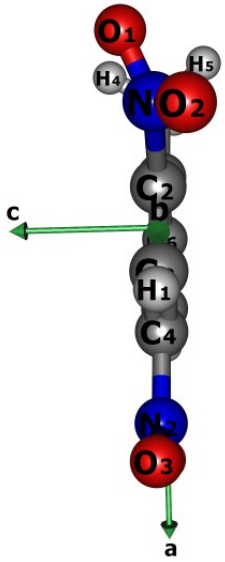

(b)

Figure 1 2,4-DNT geometry optimized at the MP2/cc-pVTZ level of theory in the *abc* principal axis system. (a) Tilted view showing the out-of-plane $-NO_2$ group and (b) View with the *ab* plane perpendicular to the figure plane.

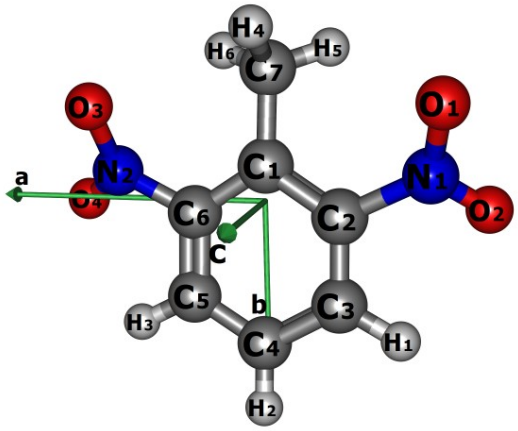

(a)

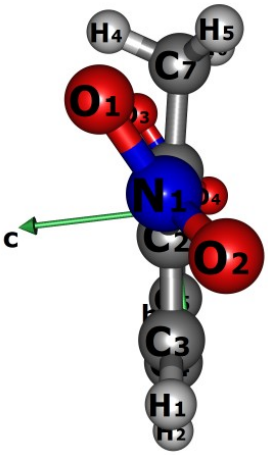

(b)

Figure 2 2,6-DNT geometry optimized at the MP2/cc-pVTZ level of theory in the *abc* principal axis system. (a) Tilted view showing the out-of-plane $-NO_2$ group and (b) View with the *ab* plane perpendicular to the figure plane.

ized in terms of the internal rotation angle α, defined as for 2,4-DNT, and of the torsional angles of the two $-NO_2$ groups: τ_1 and τ_2, respectively defined as the dihedral angles $\angle O_1N_1C_2C_1$ and $\angle O_3N_2C_6C_1$, were assumed to have opposite sign so that the O_1 and O_3 oxygen atoms are always on the same side of the phenyl ring plane. Fig. 3 depicts the qualitative surfaces for $0 \leq \alpha \leq 360°$ and $-90° \leq \tau_1 \leq 90°$. In the weak steric hindrance limiting case, six equivalent minima at $\tau_1 = 0$ and $\alpha = (i-1)60°$, with $i = 1$ to 6, arise along with 6 stationary points S_i, with $i = 1$ to 6, characterized by $\tau_1 = 7°$ ($-7°$) when i is even (odd). The geometries of the minima and stationary points are illustrated in Figs. S2 and S3 of the ESI†. The molecular configuration at each minima displays C_s symmetry with a symmetry plane containing the benzene ring. As in toluene,[23] the methyl group torsion is associated with a potential energy function displaying 6 equivalent minima. In the strong steric hindrance limiting case, six equivalent minima also arise but are characterized by different values of α and τ_1. For $\tau_1 = 90°$, $\alpha = 60$, 180, and 300°, and for $\tau_1 = -90°$, $\alpha = 0$, 120, and 240°. The molecular configuration at each minima still displays C_s symmetry but the symmetry plane is now perpendicular to the benzene ring, like in the optimized geometry of Fig. 2. The surface displays several stationary points that can be divided into 2 types. Stationary points S_i, with $i = 1$ to 6, are characterized by $\tau_1 = 0$, $\alpha = (i-1)60°$; stationary points T_i, with $i = 1$ to 6, are characterized by a lower energy and $\tau_1 = -80°$, $\alpha = 30 + (i-1)120°$, for $i = 1$ to 3, and $\tau_1 = 80°$, $\alpha = 90 + (i-4)120°$, for $i = 4$ to 6. Stationary points M_i, with $i = 1$ to 6, are maxima characterized by $\tau_1 = 0$, $\alpha = (i-1)60°$; stationary points S_i, with $i = 1$ to 6, are

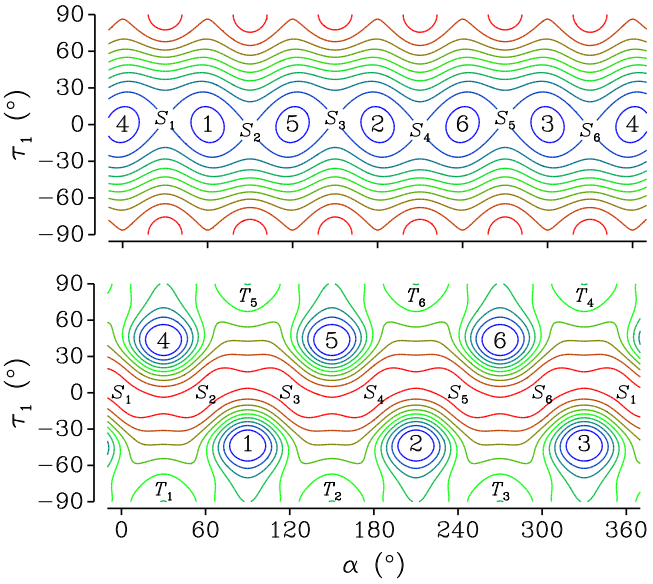

Figure 3 Contour plot of a 2-dimensional function for the 2,6-DNT isomer, qualitatively similar to the potential energy surface (see Section 4.3.2), plotted as a function of α, the methyl group angle of internal rotation, and of τ_1 and τ_2, the torsional angles of either $-NO_2$ group. τ_1 is constrained to be equal to $-\tau_2$. Minima are numbered 1 through 6. Stationary points are labeled S_i and T_i with $0 \le i \le 6$. Stationary points are labeled S_i and maxima M_i. In the upper (lower) panel steric hindrance effects are assumed to be weak (strong). Contour drawn in blue (red) correspond to low (high) energy values.

characterized by $\tau_1 = -80°$, $\alpha = 30 + (i-1)120°$, for $i = 1$ to 3, and $\tau_1 = 80°$, $\alpha = 90 + (i-4)120°$, for $i = 4$ to 6. The geometries of the minima, maxima, and stationary points are illustrated in Figs. S4 to S6 of the ESI†. In this strong steric hindrance limiting case, the surface is consistent with two tunneling motions. The first one, allowing us to connect minima 1 and 2, goes through a T-type saddle point and corresponds to a 120° rotation of the methyl group. The second one, allowing us to connect minima 1 and 4, has to overcome the barrier at M_2 and corresponds to a 60° rotation of the methyl group. Since S-type stationary points are lower in energy than M-type minima, the large amplitude motion corresponding to the first tunneling path should be more feasible.

Fig. 3 emphasizes that internal rotation in 2,6-DNT should be pictured as hindered rotation in a three fold potential. This result is numerically corroborated in Section 4.3.2 where the strong coupling case three fold potential barrier height V_3 was calculated to be 698 cm^{-1}.

2.2 Internal rotation modeling

The results presented in Sections 2.1 emphasize that both 2,4-DNT and 2,6-DNT display a torsional motion hindered by a three-fold symmetry potential. In this well known case, tunneling leads to a splitting of the rotational levels into a non-degenerate A-type and a doubly degenerate E-type sublevel.[24]

Using the barrier heights retrieved in Section 4.3, A-E torsional splittings of 84 MHz and 19 MHz were deduced for 2,4-DNT and 2,6-DNT, respectively, solving the internal rotation problem for these two molecules.[25,26] These results are consistent with the measurements since line splittings were only observed for 2,4-DNT. The theoretical treatment presented below for this species is an internal axis method (IAM) treatment,[27,28] well suited in the high-barrier limit, allowing us to compute its rotation-torsion energy levels and to perform a line frequency analysis of its microwave transitions.

This IAM treatment turns out to be numerically more stable than similar treatments designed to account for the internal rotation of a methyl group and relying on the diagonalization of a torsional Hamiltonian. Such approaches include those introduced a long time ago by Herbst *et al.*,[29] BELGI-Cs-hyperfine,[30] and XIAM.[31] In the case of a small A-E splitting they require a very large torsional basis set. In the previous investigation of Roucou *et al.*,[13] BELGI-Cs-hyperfine[30] and XIAM[31,32] failed to reproduce the FTMW spectrum of mononitrotoluene with experimental accuracy.

The IAM treatment has not been applied yet to the internal rotation of a methyl group attached to a C_s-symmetry frame like in 2,4-DNT. However, it has already been applied to many similar systems displaying hindered rotation such as ammonia dimer where we have internal rotation of the two NH_3 moieties,[33] the planar $Ar{-}H_3^+$ ion where the axis of internal rotation is perpendicular to the molecular plane,[34] monodeuterated methyl formate, exhibiting a torsional motion of an assymetrical CH_2D methyl group associated with a hindering potential with three inequivalent minima,[35] and the $Ar{-}CH_3F$ complex[36] displaying large amplitude bending and torsional motions.

The molecular model used for 2,4-DNT is based on the geometry in Fig. 1 and is illustrated in Fig. S1 of the ESI†. It consists of a methyl group attached to a planar $C_6H_3N_2O_4$ frame contained in the xz plane. The methyl group undergoes internal rotation about a fixed axis. The internal rotation of the two NO_2 groups is ignored. The angle of internal rotation α is defined in Section 2.1. The molecule fixed xyz axis system is attached to the molecule using the I^r representation. 2,4-DNT displays three C_s symmetry isoenergetic equilibrium configurations corresponding to the three equivalent minima of the hindering potential. These equilibrium configurations, identified by the integer n with $1 \le n \le 3$, are characterized by their equilibrium value of the torsional angle $\alpha_{eq}^{(n)} = 2\pi(n-1)/3$. When applying the IAM formalism,[27,28] we are led to consider two symmetry groups. The first one is C_s, the symmetry group of each equilibrium configuration, and the second one is G_6, isomorphic to C_{3v}, the symmetry group to be used for a molecule displaying internal rotation of a methyl group attached to a C_s frame.[37] In agreement with the IAM formalism, reference wavefunctions are introduced for each equilibrium configuration and expressed as:

$$\Psi_{JK\gamma n} = \phi_n(\alpha) \cdot |JK\gamma\rangle \,, \qquad (1)$$

where $\phi_n(\alpha)$ is a vibrational function centered about $\alpha_{eq}^{(n)}$ and $|JK\gamma\rangle$, with $0 \le K \le J$ and $\gamma = \pm 1$, is the Wang-type rotational function defined in Eq. (12) of Coudert and Hougen.[33] The C_s rotational symmetry species of this function is A' (A'') when $\gamma(-1)^{J+K} = +1$ (-1). Since we are dealing with the ground torsional state of 2,4-DNT, $\phi_1(\alpha)$ is an even function of α. The IAM

formalism allows us to evaluate Hamiltonian matrix elements between any two reference wavefunctions of Eq. (1):

$$H_{JK\gamma m;JK'\gamma' n} = \langle \Psi_{JK\gamma m} | H | \Psi_{JK'\gamma' n} \rangle \,, \tag{2}$$

where $1 \le m,n \le 3$ and H is the rotation-tunneling Hamiltonian. The 3 non-tunneling matrix elements with $m = n$ correspond to the rotational energy and are nonvanishing if both C_s rotational symmetry species in Eq. (2) are the same:

$$H_{JK\gamma n;JK'\gamma' n} = \langle JK\gamma | H_r | JK'\gamma' \rangle \,, \tag{3}$$

where H_r is the rotational Hamiltonian of the equilibrium configurations written using the I^r representation. The remaining matrix elements in Eq. (2) are tunneling matrix elements. Using symmetry considerations, we obtain:

$$\begin{cases} H_{JK\gamma 1;JK'\gamma' 2} = H_{JK\gamma 2;JK'\gamma' 3} = H_{JK\gamma 3;JK'\gamma' 1} \,, \\ H_{JK\gamma 2;JK'\gamma' 1} = H_{JK\gamma 3;JK'\gamma' 2} = H_{JK\gamma 1;JK'\gamma' 3} \,, \\ H_{JK\gamma 1;JK'\gamma' 2} = \gamma\gamma'(-1)^{K+K'} H_{JK\gamma 2;JK'\gamma' 1} \,. \end{cases} \tag{4}$$

These equations emphasize that all tunneling matrix elements can be related to $H_{JK\gamma 1;JK'\gamma' 2}$. In agreement with the IAM approach,[27,28] the rotational dependence of this tunneling matrix element is parameterized by three Eulerian-type angles, denoted χ_2, θ_2, and ϕ_2, that are to be computed solving Eqs. (49) of Hougen[27] for the $1 \to 2$ tunneling path. The selected path parameterization is $\alpha(t) = 2\pi(t+1)/6$, with $-1 \le t \le +1$, ensuring that $t = -1$ for equilibrium configuration 1 and $t = +1$ for equilibrium configuration 2. This corresponds to a $2\pi/3$ internal rotation of the methyl group. Using the model illustrated in Fig. S1 of the ESI†, numerically solving Eqs. (49) of Hougen[27] yields $\chi_2 = 269.474°$, $\phi_2 = 89.474°$, and $\theta_2 = 0.165°$. A detailed discussion about how these equations are solved is given in Section S1 of the ESI†. These numerical values depend on the model being considered. Using a more sophisticated model where the internal rotation of both NO_2 groups is considered would lead to small changes of these angles because the inertia moments of an NO_2 group are smaller than those of the whole molecule. It can be seen that the relation $\chi_2 = \phi_2 + \pi$ holds and can be theoretically substantiated. This relation and other results[28] allow us to write the tunneling matrix element as:

$$\begin{aligned} H_{JK\gamma 1;JK'\gamma' 2} = h_2(-1)^K [& d^{(J)}(\theta_2)_{K,K'} \cos(K+K')\phi_2 \\ & + \gamma' d^{(J)}(\theta_2)_{K,-K'} \cos(K-K')\phi_2] \,, \end{aligned} \tag{5}$$

when both C_s rotational symmetry species are the same, and as:

$$\begin{aligned} H_{JK\gamma 1;JK'\gamma' 2} = ih_2(-1)^K [& d^{(J)}(\theta_2)_{K,K'} \sin(K+K')\phi_2 \\ & + \gamma' d^{(J)}(\theta_2)_{K,-K'} \sin(K-K')\phi_2] \,, \end{aligned} \tag{6}$$

when both C_s rotational symmetry species are different. In these two equations, h_2 is a constant representing the vibrational integral in Eq. (5) of Coudert and Hougen.[28] If either K or K' is zero, the matrix element of Eqs. (5) and (6) must be divided by $2^{1/2}$. If K and K' are both zero, a division by 2 is required. The Hamiltonian matrix, setup using the reference basis functions of Eq. (1), is a $[3(2J+1)] \times [3(2J+1)]$ matrix. It can be block diagonalized into 4 submatrices using symmetry-adapted vectors of the reference wavefunctions. The matrix elements of each block will be denoted $H(\Gamma)_{JK\gamma;JK'\gamma'}$, where Γ is one of the G_6 symmetry species. The submatrices corresponding to the nondegenerate A_1 and A_2 symmetry species are of dimension $(J+1) \times (J+1)$ and $J \times J$ for J even, and of dimension $J \times J$ and $(J+1) \times (J+1)$ for J odd. Their matrix elements are given by:

$$H(\Gamma)_{JK\gamma;JK'\gamma'} = \langle JK\gamma | H_r | JK'\gamma' \rangle + 2H_{JK\gamma 1;JK'\gamma' 2} \,, \tag{7}$$

where both C_s rotational symmetry species are the same; H_r is the rotational Hamiltonian introduced in Eq. (3); and $H_{JK\gamma 1;JK'\gamma' 2}$ is given in Eq. (5). The submatrix corresponding to the E_a component of the doubly degenerate E symmetry species of G_6 is of dimension $(2J+1) \times (2J+1)$. Its matrix elements are given by:

$$H(E_a)_{JK\gamma;JK'\gamma'} = \langle JK\gamma | H_r | JK'\gamma' \rangle - H_{JK\gamma 1;JK'\gamma' 2} \,. \tag{8}$$

The matrix elements on the right should be obtained using Eqs. (3) and (5) when both C_s rotational symmetries are the same and Eq. (6) when they are different. Approximate values of the rotation-tunneling energy levels can be obtained neglecting the angular momentum arising from the torsional motion. This amounts to setting θ_2 and ϕ_2 to 0 and 90°, respectively, so that the rotation $S^{-1}(\chi_2, \theta_2, \phi_2)$ reduces to the identity matrix. With these values, Eqs. (7) and (8) yield:

$$\begin{aligned} H(A_1 \text{ or } A_2)_{JK\gamma;JK'\gamma'} &= \langle JK\gamma | H_r | JK'\gamma' \rangle + 2h_2 \delta_{K,K'} \delta_{\gamma,\gamma'} \,, \\ H(E_a)_{JK\gamma;JK'\gamma'} &= \langle JK\gamma | H_r | JK'\gamma' \rangle - h_2 \delta_{K,K'} \delta_{\gamma,\gamma'} \,. \end{aligned} \tag{9}$$

These equations mean that the rotation-tunneling energy is just the rigid-rotor energy plus a constant tunneling splitting.

The equivalent operator used for $\Delta J = 0$ matrix elements of the quadrupole coupling hyperfine Hamiltonian is written:[38]

$$H_Q = eQ\{\sum_{\beta,\gamma} J_\beta J_\gamma [q^1_{\beta,\gamma} F(\mathbf{I}_1, \mathbf{J}) + q^2_{\beta,\gamma} F(\mathbf{I}_2, \mathbf{J})]\} \,, \tag{10}$$

where β, γ run over the molecule-fixed axis system; the J_β are rotational angular momentum components; $q^1_{\beta,\gamma}$ and $q^2_{\beta,\gamma}$ are components of the electric field gradient at nitrogen atoms N_1 and N_2; $\mathbf{I}_1$ and $\mathbf{I}_2$ are their nuclear spin angular momentum; and $F(\mathbf{I}_j, \mathbf{J})$ is an operator corresponding to the Casimir function. The hyperfine Hamiltonian in this equation only has non-tunneling matrix elements between two reference wavefunctions of Eq. (1) characterized by the same value of n. The coupling scheme used for the total nuclear spin rotational wavefunction is given in Section 4.1 and the relevant matrix elements in Robinson and Cornwell.[39]

3 Experimental setup

The pure rotational spectra of 2,4-DNT and 2,6-DNT were recorded in the microwave range (2–20 GHz) using an FP-FTMW spectrometer coupled to a pulsed supersonic jet already detailed elsewhere.[40,41] Powder samples of 2,4-DNT (97% purity) and 2,6-DNT (98% purity) were purchased from Sigma-Aldrich and used without further purification. About 0.2 g of DNT were placed into the reservoir of an injector,[42] heated at 423 K

(P_{vap} = 19.0 mbar and 9.2 mbar for 2,4-DNT and 2,6-DNT, respectively[43]) and pressurized under 4 bar of neon used as buffer gas. The gas mixture was injected into the cavity during a short opening (800 μs) of a 1 mm internal diameter orifice (series 9 pulse valve) at a repetition rate of 1 Hz to create a supersonic jet of vibrationally and rotationally frozen molecules (T_{rot} of a few K). They were polarized by a 2 μs microwave pulse carrying an energy adjusted to be close to the $\pi/2$ condition. A heterodyne detection lowers the frequency of the free induction decays (FIDs) down to 30 MHz, further digitized by an acquisition device operating at a sampling rate of 120 MHz. The spectrometer can be operated in a scan mode: it is successively tuned to frequencies incremented (or decremented) by 250 kHz. The portions of spectra recorded at each frequency are then coadded to simulate a continuous scan spectrum. In the precise measurement mode, the lines were digitized over 65 536 to 131 072 points which led to a frequency grid of 1.84 to 0.92 kHz. Lines were observed as two Doppler components, due to the coaxial arrangement of the FP cavity and of the supersonic jet. The frequency of the transitions were determined as the arithmetic average of the frequencies of the two Doppler components. For well resolved and isolated lines, the accuracy of the measurements is estimated to 2 kHz. In the case of a congested hyperfine structure, the accuracy may fall down to 4 kHz.

4 Results and Discussion

4.1 Spectra Analysis

The spectra of 2,4- and 2,6-DNT were assigned by scanning around the frequencies predicted from the calculated rotational constants (see Section 2.1). Low J values transitions were readily found. Updated fits were used to predict the positions of new transitions characterized by a higher J-value.

The rotational transitions of both 2,4- and 2,6-DNT display a hyperfine structure resulting from nuclear quadrupole coupling (NQC) at the two ^{14}N nuclei. Transitions were assigned in terms of rotational and hyperfine quantum numbers as $J'_{K'_aK'_c}I'F' \leftarrow J''_{K''_aK''_c}I''F''$, corresponding to the coupling scheme $\mathbf{I} = \mathbf{I}_1 + \mathbf{I}_2$ and $\mathbf{F} = \mathbf{I} + \mathbf{J}$. The selection rules for the most intense lines being $\Delta F = \Delta J$, each rotational transition is split into up to 9 hyperfine components. Hyperfine patterns were fully resolved only in a few cases, for low J values and / or when $K_a \approx J$. Examples of well resolved hyperfine structures are shown in Figs. 4a and 4b. Assignment of the hyperfine components was based on the hyperfine structure as simulated with the NQC constants computed at the B98/cc-pVTZ level of theory.

For 2,4-DNT, 293 a- and b-type lines from $J = 3$ up to $J = 19$ and $K_a = 5$ were assigned. In many cases, internal rotation splittings could be observed. Fig. 4c shows a well resolved internal rotation splitting for one of the hyperfine components of the $8_{26} \leftarrow 7_{17}$ transition. Preliminary analyses with the internal rotation approach of Section 2.2 were carried out for the assignment in terms of A- and E-type torsional components. For 2,6-DNT, only b-type lines are allowed due to its two-fold symmetry axis (see Fig. 2), 255 transitions were assigned from $J = 3$ up to $J = 18$ and $K_a = 6$. No internal rotation splittings were observed. The experimental frequencies of the measured transitions are listed in Tables S1 and S2 (ESI†) for respectively 2,4- and 2,6-DNT.

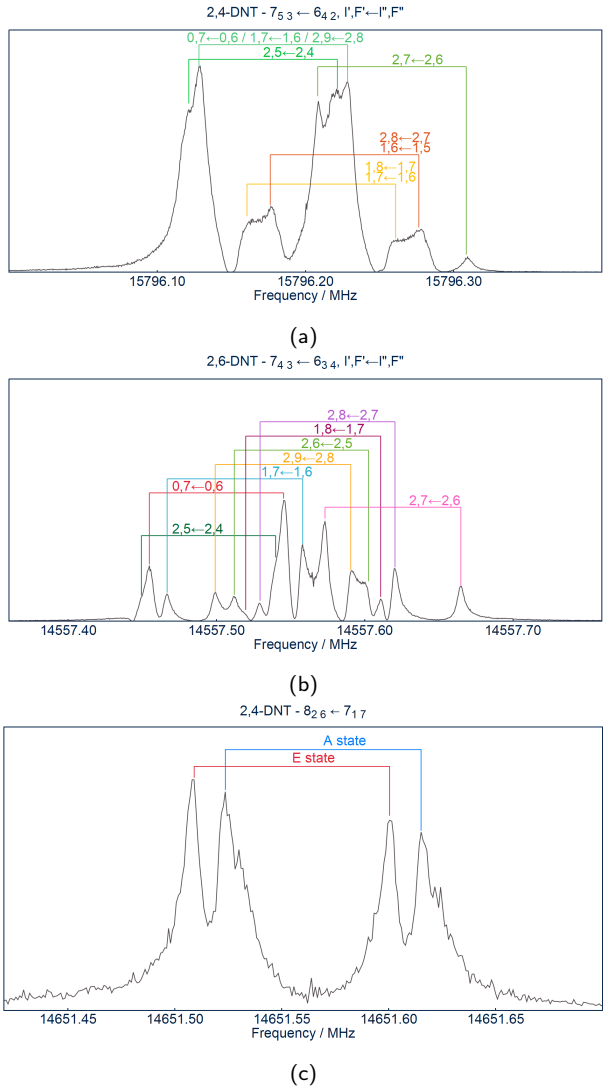

Figure 4 Experimental microwave spectrum (a) for $7_{53} \leftarrow 6_{42}$ transition of 2,4-DNT, A-E splitting non-resolved; (b) $7_{43} \leftarrow 6_{34}$ transition of 2,6-DNT. Doppler doublets have been assigned in terms of hyperfine quantum numbers as $I'F' \leftarrow I''F''$; (c) An isolated hyperfine component of the $8_{26} \leftarrow 7_{17}$ transition of 2,4-DNT displaying a 15 kHz A-E splitting due to the internal rotation of the methyl group, hyperfine structure non-resolved.

4.1.1 Semi-rigid Hamiltonian analysis

The transitions assigned for 2,4-DNT involving A-type torsional levels and all the transitions assigned for 2,6-DNT were fitted using an asymmetric rotor Watson-type Hamiltonian set up in the A-reduction and I^r representation. For both isomers, the rotational energies and the hyperfine structure were accounted for using the SPFIT/SPCAT programs of the CALPGM suite written by Pickett.[44,45] Due to the symmetric positions of the two ^{14}N nuclei in 2,6-DNT, their diagonal effective NQC constants were constrained to be equal.

The spectroscopic parameters obtained for both isomers are reported in Table 1. The experimental rotational constants are generally in good agreement with their calculated values retrieved in Section 2.1; the discrepancies are at most 2%. Concerning the

Table 1 Rotational and NQC constants of 2,4-DNT and 2,6-DNT obtained from the MW fit described in Section 4.1.1 with SPFIT/SPCAT and compared with quantum chemical calculations.

	2,4-DNT					2,6-DNT				
Parameter[a]	Experimental[b]	MP2	Dev.	DFT	Dev.	Experimental[b]	MP2	Dev.	DFT	Dev.
A / MHz	1488.045 103(221)	1498.78	0.72	1487.95	−0.01	1558.897 175(90)	1555.57	−0.21	1577.02	1.16
B / MHz	549.027 072(74)	549.44	0.08	551.11	0.38	583.559 817(96)	588.59	0.86	581.33	−0.83
C / MHz	409.378 468(37)	412.39	0.74	407.29	0.51	448.759 347(54)	454.20	1.21	443.79	−1.11
Δ_J/ kHz	0.007 09(46)	0.0075		0.0068		0.009 79(44)	0.0001		0.0001	
Δ_{JK}/ kHz	0.0077(33)	0.0065		0.0043		0.013 57(181)	0.0001		0.0001	
Δ_K/ kHz	0.0687(56)	0.10		0.08		0.069 11(158)	0.07		0.05	
δ_J/ kHz	0.001 583(213)	0.0018		0.0016		0.000 898(234)	0.0011		0.0001	
δ_K/ kHz	0.0289(40)	0.32		0.30		0.0412(50)	0.04		0.05	
N_1										
χ_{aa}/MHz	−0.5618(127)	−0.195		−0.576		−0.7221(34)	−0.371		−0.859	
χ_{bb}/MHz	−0.1715(32)	0.025		−0.428		0.1222(132)	0.177		−0.029	
χ_{cc}/MHz	0.733(32)	0.170		1.005		0.5998(132)	0.193		0.888	
N_2										
χ_{aa}/MHz	−0.6763(113)	−0.368		−0.958		−0.7221(34) [d]	−0.371		−0.859	
χ_{bb}/MHz	0.0484(33)	0.453		−0.227		0.1222(132) [d]	0.177		−0.029	
χ_{cc}/MHz	0.6280(33)	−0.086		1.185		0.5998(132) [d]	0.193		0.888	
$\lvert\mu_a\rvert$[c] / D	y	1.30		1.51		n	0.00		0.00	
$\lvert\mu_b\rvert$[c] / D	y	4.11		4.62		y	2.75		2.87	
$\lvert\mu_c\rvert$[c] / D	n	0.20		0.17		n	0.33		0.23	
σ_{fit} / kHz	1.95					2.28				
WRMS/unitless	0.90					0.92				
N_{lines}	239					255				

[a] A, B, C are the ground state rotational constants; Δ_J to δ_K are the five quartic centrifugal distortion constants; χ_{ii} the diagonal NQC constants; $|\mu_i|$ the permanent dipole components; σ_{fit} is the standard deviation of the fit; WRMS is the unitless weighted root-mean-square and N_{lines} are the number of transitions included in the fit.

[b] Numbers in parentheses are standard errors (1σ) in units of the last digit.

[c] y and n indicate if the x-type transitions are observed or not observed, respectively.

[d] Due to the C_{2v} symmetry of 2,6-DNT, the quadrupole coupling constants of N_2 were constrained to the values of N_1 during the fitting procedure.

NQC constants, large differences can be observed between those computed using the DFT method (B98/cc-pVTZ) and the *ab initio* (MP2/cc-pVTZ) values. This result is not unexpected since the DFT method provides us with reliable values for NQC constants, usually within a few % of their experimental values, and this method is adopted when investigating hyperfine splittings in MW spectra. *Ab initio* calculations tend to fail for accurately predicting NQC constants in the case of a nitro group, as emphasized by the present analysis and by our previous one about nitrotoluene isomers.[13,16]

4.1.2 Internal rotation analysis

In this analysis, transitions of 2,4-DNT involving *A*- and *E*-type torsional levels were fitted with the theoretical treatment of Section 2.2. A total of 285 lines were reproduced with a unitless standard deviation of 1.6, varying 12 spectroscopic parameters reported in Table 2. As expected, the rotational constants in this table agree quite well with those in Table 1 for 2,4-DNT; both sets agree within 0.1 MHz. For the NQC constants, the agreement is less satisfactory as, although the differences between both sets of parameters are also on the order of 0.1 MHz, these parameters are on the order of 0.5 MHz. The agreement is also less satisfactory for distortion constants, but this is due to the fact that energies are not computed using the same theoretical treatment. As emphasized by Table 2, the tunneling parameters h_2 and ϕ_2 could be determined, but not θ_2 which was constrained to its theoretical value (Section 2.2). The satisfactory agreement between the theoretical (Section 2.2) and experimental values of ϕ_2 indicates that the IAM tunneling model well describes 2,4-DNT. The value retrieved for h_2 is negative as expected for the ground torsional state. This value is consistent with an *A*-*E* tunneling splitting of $3|h_2| = 87$ MHz. Although such a value far exceeds the experimental resolution of the spectrometer used in this work, the line splittings are nonetheless difficult to resolve because they depend on the difference between the upper and lower levels tunneling splitting. When the angular momentum due to the torsional motion is neglected, the tunneling splitting is given by Eqs. (9) which is consistent with a constant level splitting and no line splitting. As emphasized by Eqs. (5) and (6), a rotational dependence of the tunneling splitting does take place and leads to the small line splittings observed in this work. Solving the internal rotation problem for 2,4-DNT,[25,26] the observed value of the *A*-*E* splitting was found to be consistent with an experimental height of $524.7(120)\,\mathrm{cm}^{-1}$ for the hindering potential barrier V_3. This value agrees reasonably well with that reported in Section 4.3. The observed minus calculated table for the present analysis can be found in Table S3 of the ESI†.

Table 2 Spectroscopic parameters determined with the tunneling approach of Section 2.2 for 2,4-DNT.

Parameter[a]	Experimental[b]	Parameter[a]	Experimental[b]
θ_2 / °	0.165[b]	N_1	
ϕ_2 / °	89.928(7)	χ_{aa} / MHz	−0.686[d]
h_2 / MHz	−29.029(2700)[c]	χ_{bb} / MHz	−0.076(10)
		χ_{cc} / MHz	0.754(10)
A / MHz	1488.045 189(210)		
B / MHz	549.026 300(39)	N_2	
C / MHz	409.378 461(42)	χ_{aa} / MHz	−0.560[d]
		χ_{bb} / MHz	−0.047(12)
Δ_K / Hz	78.258(6500)	χ_{cc} / MHz	0.605(9)
Δ_{KJ} / Hz	14.632(2300)		
Δ_J / Hz	3.801(81)	σ_{fit} / kHz	6.1
		WRMS[e]	1.5
		N_{lines}	197

[a] Parameters are defined in Eqs. (3), (5), (6), and (10). The effective quadrupole coupling tensor components $\chi_{\beta,\gamma}$ are equal to $eQq_{\beta,\gamma}$.
[b] In MHz except for θ_2 and ϕ_2 which are in degrees.
[c] Constrained value to those determined in Section 2.2.
[d] The value of h_2 is consistent with a value of the hindering potential barrier V_3 of $524.7(120)\,\mathrm{cm}^{-1}$.
[e] Constrained values to have : $\chi_{aa}+\chi_{bb}+\chi_{cc}=0$.
[f] The weighted RMS is unitless.

4.2 Molecular electrostatic surface potential

In order to understand the variations of the methyl group torsional barrier V_3 for mono- and dinitrotoluene isomers, molecular electrostatic potentials mapped at the isosurface having an electron density $0.001\,\mathrm{e\,Å}^{-3}$ were calculated at the ωB97XD/6-311+G(2df,2p) level of theory[46–48] and created using Spartan Software.[49]

The results in Section 4.1 and those reported in Ref. 13 reveal that V_3 is significantly lower in 2,4-DNT than in 2-NT, it decreases from $563\,\mathrm{cm}^{-1}$ in the latter to $525\,\mathrm{cm}^{-1}$ in the former. This decrease by adding a second nitro group in para position highlights the influence of an additional electronic effect ($-NO_2$ resonance) which seems to counterbalance the steric effect of the nitro group in ortho position. With a higher V_3 barrier expected for 2,6-DNT, we can assume that if the second nitro group is also located in a neighboring position of the $-CH_3$, steric effects, which increase the barrier height, become again dominant compared to the electronic effects. Knowledge of the electrophilic and nucleophilic areas in explosive taggants, NT and DNT isomers, will help understand the variation of the torsional barrier height, as well as their ability to interact with other molecules. The nitro group has a strong electron-withdrawing inductive effect (-I). This effect is highlighted in Fig. 5 where molecular electrostatic potential surfaces are shown for the three isomers of NT and the two isomers of DNT. The presence of the second nitro moiety in DNT isomers modifies the electronic distribution and affects the electronic density of the benzene rings, making them nucleophilic. Indeed, the additional $-NO_2$ group in the two DNT isomers further depletes the electronic density of the benzene ring. If we compare 2-NT and 2,4-DNT (Fig. 5 (a) and (d)), in the vicinity of the methyl group, the steric effect may be assumed equivalent but the higher electronic density in the ring of 2-NT increases the hindering barrier height. Comparing the two DNT isomers (Fig. 5 (d) and (e)), the electronic density is slightly lower in the 2,6-DNT ring but the steric effects are accentuated with the two $-NO_2$ groups on both sides of the methyl group.

4.3 Dynamic interaction of functional groups

An accurate evaluation of the methyl group torsional potential energy function (PEF) in 2,4-DNT and 2,6-DNT requires account-

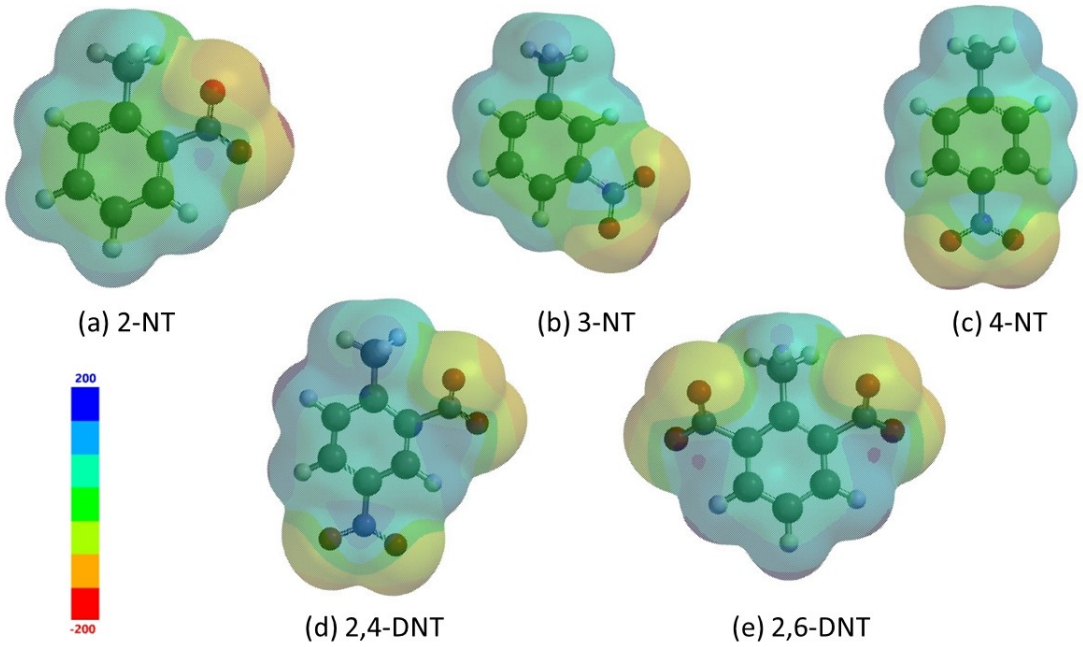

Figure 5 Molecular electrostatic potentials calculated at the ωB97XD/6-311+G(2df,2p) level of theory for three mononitrotoluene isomers and two dinitrotoluene isomers.

ing for the interaction between the $-CH_3$ and $-NO_2$ functional groups because of their immediate proximity. Following the same procedure as for nitrotoluenes,[13] two dimensional potential energy surfaces (2-D PES) were calculated at the B98/cc-pVTZ level of theory and parameterized in terms of the $-CH_3$ and $-NO_2$ groups dihedral angles, all other geometrical parameters being optimized at each step.[50] In these calculations, a minimal description in which these angles span respectively a 120° and a 180° angular range was first obtained. A full description was retrieved afterwards using the 3- and 2-fold symmetry of these groups. The DFT energy points were fitted to a 2-D trigonometric expension written in terms of sines and cosines of the two dihedral angles. This expansion was used to search for the stationnary points and for the minimum energy paths (MEP). In the high barrier limit, the latters provide us with information about the energy level diagram of the molecule since it tunnels along these paths when connecting two minima of the potential energy surface.[51]

4.3.1 2,4-DNT

For the 2-D PES of 2,4-DNT, 898 points were calculated and fitted to the trigonometric expansion using 23 parameters. The DFT energies were reproduced with a root mean square deviation of $8.1\,cm^{-1}$. Fig. 6 shows the 2-D PES along the $-CH_3$ and $-NO_2$ torsional angles α and τ_1. The surface displays 6 equivalent minima occuring in pairs. Theses pairs are identified by n, with $1 \leq n \leq 3$, and consist of two close lying minima characterized by $\alpha = (n-1)120 \pm 12°$ and $\tau_1 = \pm 24°$. The barrier height between minima of the same pair is $60\,cm^{-1}$. The geometry of these minima is similar to those of 2-NT where the "twisted" equilibrium geometry of both groups also leads to C_1 equilibrium configurations with no symmetry plane.[13] 3 local maxima and 6 saddle points can also be seen in the surface as well as two MEP labeled I and II. The geometries of the minima, stationary points, and local maxima are illustrated in Figs. S7 to S9 of the ESI†. MEP I (MEP II) connects the surface minima and the S saddle points with $\tau_1 > 0$ ($\tau_1 < 0$). Cuts of the 2-D PES along the MEP yield the PEF and the torsional angle τ_1 as a function of α. Both PEF are plotted in Fig. 7 which emphasizes that they display 120° periodicity, but are not even functions of α. The barrier height between minima is $563\,cm^{-1}$. Fig. 6 emphasizes that along MEP I, τ_1 varies slowly between 24° at the minima and 40° at the saddle points S. For MEP II, these values should be changed into their negative. A cut of the surface along the tunneling motion connecting the two minima of Pair 1 is shown in Fig. S14 of the ESI†. The height of the barrier between the two minima is as expected $60\,cm^{-1}$.

The barrier height retrieved from the 1-D model of Section 2.2 cannot be compared to that retrieved from the MEP of the present 2-D surface because this surface, characterized by shallow minima, does not correspond to the high barrier limit. As already stressed, the barrier height between minima belonging to the same pair has a low value of only $60\,cm^{-1}$. A PEF for the $-CH_3$ torsion was computed using an alternative adiabatic approach where the Schrödinger equation for the $-NO_2$ torsion was solved for each value of the torsional angle α. The results are shown in Fig. 7 displaying the variations with α of the lowest eigenvalue. A PEF with 120° periodicity which is an even function of α arises. The barrier height, slightly lower than with MEP I and II, is $515\,cm^{-1}$. The fast variations observed near $\alpha = 60°$, 180°, and 300° are due to avoided crossings.

4.3.2 2,6-DNT

In 2,6-DNT, the vibrational dynamics is more complicated since we have a 3-D PES depending on the $-CH_3$ and $-NO_2$ groups dihedral angles α, τ_1, and τ_2. A thorough investigation of this

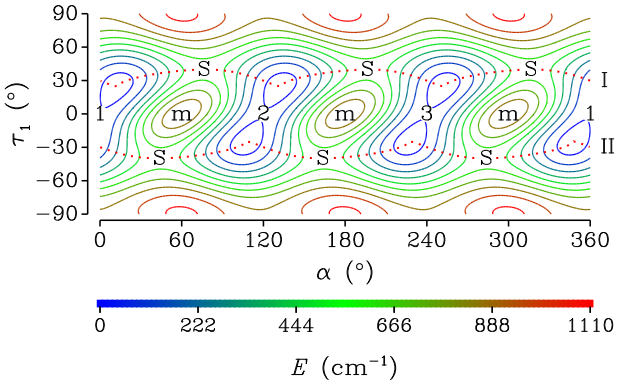

Figure 6 2-D PES of 2,4-DNT calculated at the B98/cc-pVTZ level of theory along the $-CH_3$ and $-NO_2$ torsional angles α and τ_1, respectively. The relative energy ranges from 0 to 1110 cm^{-1}. Contour lines corresponding to equally spaced energy values from 55 to 1054 cm^{-1} are shown. Numbers 1, 2, and 3 label the three pairs of equivalent minima; m is a local maximum; S is a saddle point. Two MEP are drawn using dotted lines and identified with I and II.

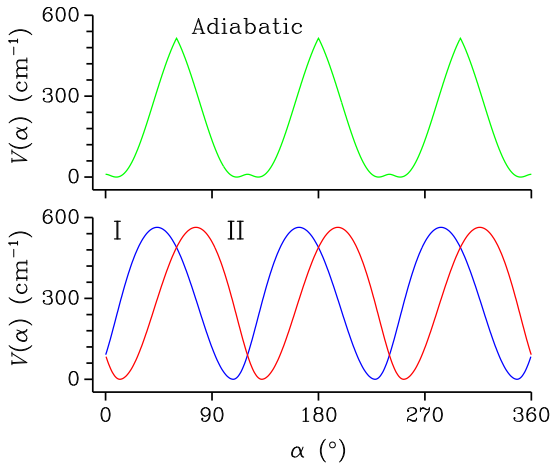

Figure 7 PEF in cm^{-1} as a function of α obtained for 2,4-DNT. The lower panel shows the PEF corresponding to MEP I and II of the surface in Fig. 6. The upper panel shows the PEF calculated from the same surface, but with the adiabatic approach.

surface is beyond the scope of the present paper. Instead, two 2-D surfaces were studied reducing the 3-D problem to a 2-D one.

In the first surface, the angles τ_1 and τ_2 were constrained to fulfill the relation $\tau_1 = -\tau_2$. 958 DFT points were calculated and fitted to the trigonometric expansion with an RMS of 15.1 cm^{-1}, using 77 parameters. The surface, shown in Fig. 8, displays 6 minima numbered 1 through 6. For minima 1 to 3, α is 90°, 210°, and 330°, and $\tau_1 = 38°$; and for minima 4 to 6, α is shifted by 60° and τ_1 is changed into its negative value. The surface is qualitatively similar to that in Fig. 3 for the strong steric hinderence limit as they both exhibit the same stationnary points. The geometries of the minima, stationary points, and maxima of the present surface are illustrated in Figs. S10 to S12 of the ESI†. The present surface displays two MEP, identified by I and II, which are almost horizontal. The PEF along MEP I is plotted in Fig. 9 and we have a three-fold symmetry potential with a barrier height V_3 of 698 cm^{-1}. Fig. 8 corresponds to the high barrier limit as potential barriers ranging from 698 to 1600 cm^{-1} arise between minima. The energy levels of 2,6-DNT can, therefore, be well described assuming a torsional motion of the methyl group hindered by a 3-fold symmetry potential. A value of $\tau_1 = -\tau_2 = 38°$ ensures that the oxygen atoms of the NO_2 groups which are the closest to the methyl group remain far away from that group. There is little adjustment of either NO_2 group when the methy group rotates, as confirmed by nearly straight MEP's. A cut of the surface along the tunneling motion connecting minima 1 and 4 is shown in Fig. S15 of the ESI† and the barrier arising between each minima displays a height of 1600 cm^{-1}. The oxygen atoms of the NO_2 groups which are the closest to the methyl group always stay on the same side of the phenyl ring symmetry plane because going on the other side requires overcoming the 1600 cm^{-1} high barrier.

The second surface is a relaxed one where the energy was minimized with respect to τ_2 for each value of α and τ_1. The 919 DFT points thus found were fitted to the trigonometric expansion with an RMS of 7.7 cm^{-1}, using 77 parameters. The surface is shown in Fig. 10 and it can be seen that the region with $10° \leq \tau_1 \leq 90°$ is quite analogous to the same region in the previous surface (Fig. 8) while the region with $-90° \leq \tau_1 \leq 10°$ is not. This stems from the fact that in the former region the quantum chemical calculations yields a negative τ_2 such that $\tau_1 \sim -\tau_2$; in the latter region this approximate relation no longer holds because the quantum chemical calculations still yields a negative value for this torsional angle. The PEF along the only MEP arising with the present surface is plotted in Fig. 9 and barely differs from the PEF along MEP I of the previous surface. Both PEF are consistent with a barrier height $V_3 = 698$ cm^{-1}. The geometry of the minima and stationary points of the relaxed surface are quite similar to those of the previous surface. The geometries of the maxima are not and those obtained with the present surface are shown in Fig. S13 of the ESI†.

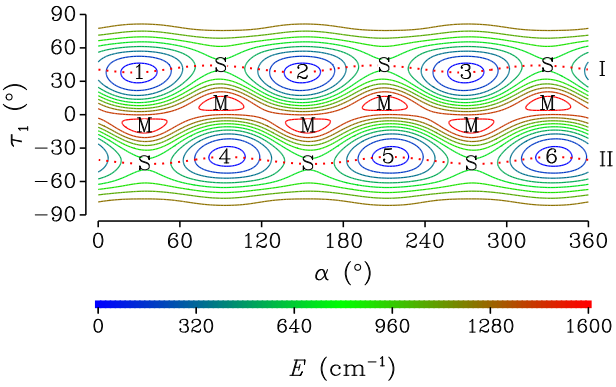

Figure 8 2-D PES of 2,6-DNT calculated at the B98/cc-pVTZ level of theory along the $-CH_3$ and $-NO_2$ torsional angles α and $\tau_1 (= -\tau_2)$, respectively. The relative energy ranges from 0 to 1600 cm^{-1}. Contour lines corresponding to equally spaced energy values from 80 to 1520 cm^{-1} are shown. Numbers 1 to 6 label the six energetically equivalent minima; M is the surface maximum; S is a saddle point. Two MEP are drawn using dotted lines and identified with I and II.

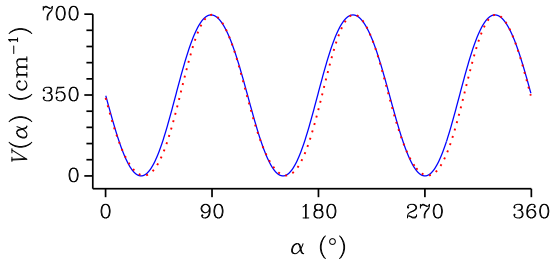

Figure 9 PEF in cm^{-1} of 2,6-DNT as a function of α obtained from 2-D surfaces. Solid lines are used for the PEF arising from the surface computed with the constraint $\tau_1 = -\tau_2$ shown in Fig. 8. Dotted lines are used for the relaxed surface shown in Fig. 10.

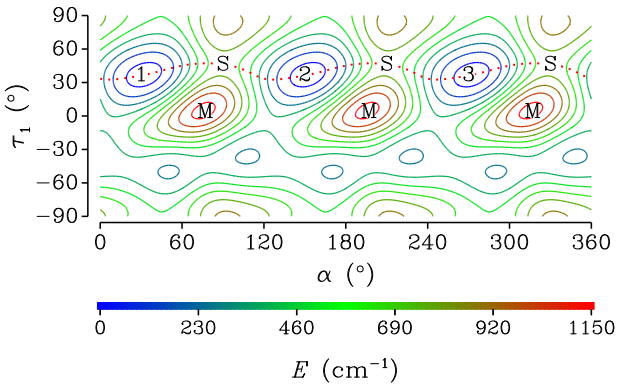

Figure 10 Relaxed 2-D PES of 2,6-DNT calculated at the B98/cc-pVTZ level of theory along the $-CH_3$ and $-NO_2$ torsional angles α and τ_1, respectively. The energy is minimized with respect to the torsional angle τ_2. The relative energy ranges from 0 to $1150\,cm^{-1}$. Contour lines corresponding to equally spaced energy values from 57.5 to $1092.5\,cm^{-1}$ are shown. Numbers 1, 2, and 3 label the three minima; M is the maximum; S is a saddle point. The MEP is drawn using dotted lines.

5 Conclusion

The microwave spectra of the 2,4-DNT and 2,6-DNT isomers of dinitrotoluene were recorded using an FP-FTMW spectrometer allowing us to measure several hundred lines for each species. Due to their very low vapor pressure at room temperature, to record a spectrum in a static cell experiment represents a challenge. In agreement with DFT and *ab initio* calculations, both species display internal rotation of their $-CH_3$ methyl group coupled to that of the $-NO_2$ groups. According to B98/cc-pVTZ calculations, the height of the barriers hindering the methyl group internal rotation were found to be 515 and $698\,cm^{-1}$ for 2,4-DNT and 2,6-DNT, respectively. For 2,4-DNT, the fact that the barrier is smaller than in 2-NT could be qualitatively understood in Section 4.3 comparing molecular electronic surface potentials. The higher barrier obtained for 2,6-DNT than for 2,4-DNT is due to steric hindrance effects from both $-NO_2$ groups and it was shown qualitatively in Section 2.1 that these effects alter the nature of the internal rotation hindering potential from the expected 6-fold symmetry to a 3-fold symmetry. These results were numerically substantiated in Section 4.3.2.

The measurements are consistent with the calculated torsional barrier heights since *A*-*E* internal rotation splittings could be observed for 2,4-DNT but not for 2,6-DNT. The observed frequencies of both species were first fitted using a semi rigid rotator Hamiltonian including hyperfine splittings due to the nuclear quadrupole coupling from both nitrogen atoms. In a subsequent analysis, the transitions of 2,4-DNT only were fitted using an approach accounting for the methyl group internal rotation and *A*- and *E*-type lines were included in the data set. This second analysis allowed us to retrieve an accurate value of the rotationless *A*-*E* tunneling splitting which could be extracted from the rotational dependence of the tunneling splitting. This observed value allowed us to retrieve an experimental value of $525\,cm^{-1}$ for the internal rotation barrier height which compares favorably with the calculated value.

The spectroscopic parameters fitted to the FP-FTMW experimental frequencies will allow us to build room-temperature rotational line lists in the mm-wave spectral domain. An intra-cavity mm-wave spectrometer is presently being built thanks to recent technological development at the Laboratory of Physical Chemistry of the Atmosphere (LPCA) allowing Cavity Enhanced Absorption Spectroscopy (CEAS) [52] and Cavity Ring Down Spectroscopy (CRDS) [53] in the terahertz spectral domain. This spectrometer, shown in Refs. 13,16 to have a sensitivity sufficient to measure room-temperature mononitroluene in the mm-wave domain, will be applied to the detection of the even less volatile DNT species thanks to the results of the present investigation.

Conflicts of interest

There are no conflicts to declare.

Acknowledgments

This work received financial support from the French Agence Nationale de la Recherche via funding of the project Millimeter-wave Explosive Taggant vapors Investigations using Spectral taxonomy (METIS) under contract number ANR-20-ASTR-0016-03. LPCA and PhLAM laboratories are members of the Laboratory of Excellence CaPPA (Chemical and Physical Properties of the Atmosphere) funded by the French National Research Agency (ANR) through the PIA (Programme d'Investissements d'Avenir) under Contract No. ANR-11-LABX-005-01.

Notes and references

1 T. D. Schachel, A. Stork, R. Schulte-Ladbeck, T. Vielhaber and U. Karst, *Forensic Sci. Int.*, 2020, **308**, 110180.
2 C. A. Cruse and J. V. Goodpaster, *Forensic Chem.*, 2021, **26**, 100362.
3 S. Elbasuney and Y. H. El-Sharkawy, *TrAC - Trends Anal. Chem.*, 2018, **108**, 269–277.
4 A. G. Davies, A. D. Burnett, W. Fan, E. H. Linfield and J. E. Cunningham, *Mater. Today*, 2008, **11**, 18–26.
5 E. M. Witko and T. M. Korter, *J. Phys. Chem. A*, 2012, **116**, 6879–6884.
6 M. Mäkinen, M. Nousiainen and M. Sillanpää, *Mass Spectrom. Rev.*, 2011, **30**, 940–973.
7 I. A. Buryakov, *J. Anal. Chem.*, 2011, **66**, 674–694.
8 V. A. Kostarev, G. E. Kotkovskii, A. A. Chistyakov and A. E. Akmalov, *Talanta*, 2022, **245**, 123414.

9 W. Zhang, Y. Tang, A. Shi, L. Bao, Y. Shen, R. Shen and Y. Ye, *Materials*, 2018, **11**, 1364.

10 M. B. Pushkarsky, I. G. Dunayevskiy, M. Prasanna, A. G. Tsekoun, R. Go and C. K. N. Patel, *Proc. Natl. Acad. Sci. U.S.A.*, 2006, **103**, 19630–19634.

11 M. Snels, T. Venezia and L. Belfiore, *Chem. Phys. Lett.*, 2010, **489**, 134–140.

12 M. A. Martin-Drumel, A. Roucou, G. G. Brown, S. Thorwirth, O. Pirali, G. Mouret, F. Hindle, M. C. McCarthy and A. Cuisset, *J. Chem. Phys.*, 2016, **144**, 084305.

13 A. Roucou, M. Goubet, I. Kleiner, S. Bteich and A. Cuisset, *ChemPhysChem*, 2020, **21**, 2523–2538.

14 A. Roucou, D. Fontanari, G. Dhont, A. Jabri, C. Bray, F. Hindle, G. Mouret, R. Bocquet and A. Cuisset, *ChemPhysChem*, 2018, **19**, 1572–1578.

15 P. Asselin, J. Bruckhuisen, A. Roucou, M. Goubet, M.-A. Martin-Drumel, A. Jabri, Y. Belkhodja, P. Soulard, R. Georges and A. Cuisset, *J. Chem. Phys.*, 2019, **151**, 194302.

16 A. Roucou, I. Kleiner, M. Goubet, S. Bteich, G. Mouret, R. Bocquet, F. Hindle, W. L. Meerts and A. Cuisset, *ChemPhysChem*, 2018, **19**, 1056–1067.

17 R. J. Foltynowicz, R. E. Allman and E. Zuckerman, *Chem. Phys. Lett.*, 2006, **431**, 34–38.

18 M. J. Frisch, G. W. Trucks, H. B. Schlegel, G. E. Scuseria, M. A. Robb, J. R. Cheeseman, G. Scalmani, V. Barone, G. A. Petersson, H. Nakatsuji, X. Li, M. Caricato, A. V. Marenich, J. Bloino, B. G. Janesko, R. Gomperts, B. Mennucci, H. P. Hratchian, J. V. Ortiz, A. F. Izmaylov, J. L. Sonnenberg, D. Williams-Young, F. Ding, F. Lipparini, F. Egidi, J. Goings, B. Peng, A. Petrone, T. Henderson, D. Ranasinghe, V. G. Zakrzewski, J. Gao, N. Rega, G. Zheng, W. Liang, M. Hada, M. Ehara, K. Toyota, R. Fukuda, J. Hasegawa, M. Ishida, T. Nakajima, Y. Honda, O. Kitao, H. Nakai, T. Vreven, K. Throssell, J. A. Montgomery, Jr., J. E. Peralta, F. Ogliaro, M. J. Bearpark, J. J. Heyd, E. N. Brothers, K. N. Kudin, V. N. Staroverov, T. A. Keith, R. Kobayashi, J. Normand, K. Raghavachari, A. P. Rendell, J. C. Burant, S. S. Iyengar, J. Tomasi, M. Cossi, J. M. Millam, M. Klene, C. Adamo, R. Cammi, J. W. Ochterski, R. L. Martin, K. Morokuma, O. Farkas, J. B. Foresman and D. J. Fox, *Gaussian 16 Revision B.01*, 2016, Gaussian Inc. Wallingford CT.

19 C. Møller and M. S. Plesset, *Phys. Rev.*, 1934, **46**, 618–622.

20 H. L. Schmider and A. D. Becke, *J. Chem. Phys.*, 1998, **108**, 9624–9631.

21 T. H. Dunning Jr, *J. Chem. Phys.*, 1989, **90**, 1007–1023.

22 N. W. Larsen, *J. Mol. Struc.*, 2010, **963**, 100–105.

23 V. V. Ilyushin, Z. Kisiel, L. Pszczókowski, H. Mäder and J. T. Hougen, *J. Mol. Spectrosc.*, 2010, **259**, 26–38.

24 H. V. L. Nguyen and I. Kleiner, *Phys. Sci. Rev.*, 2022, **7**, 679–726.

25 C. C. Lin and J. B. Swalen, *Rev. Mod. Phys.*, 1959, **31**, 841–892.

26 R. M. Lees and J. G. Baker, *J. Chem. Phys.*, 1968, **48**, 5299–5318.

27 J. T. Hougen, *J. Mol. Spectrosc.*, 1985, **114**, 395–426.

28 L. H. Coudert and J. T. Hougen, *J. Mol. Spectrosc.*, 1988, **130**, 86–119.

29 E. Herbst, J. K. Messer, F. C. De Lucia and P. Helminger, *J. Mol. Spectrosc.*, 1984, **108**, 42–57.

30 I. Kleiner, *J. Mol. Spectrosc.*, 2010, **260**, 1–18.

31 H. Hartwig and H. Dreizler, *Zeitschrift für Naturforschung A*, 1996, **51**, 923–932.

32 R. C. Woods, *J. Mol. Spectrosc.*, 1967, **22**, 49–59.

33 L. H. Coudert and J. T. Hougen, *J. Mol. Spectrosc.*, 1991, **149**, 73–98.

34 S. Bailleux, M. Bogey, H. Bolvins, S. Civiš, M. Cordonnier, A. F. Krupnov, M. Y. Tretyakov, A. Walters and L. H. Coudert, *J. Mol. Spectrosc.*, 1998, **190**, 130–139.

35 L. Margulès, L. H. Coudert, H. Møllendal, J.-C. Guillemin, T. R. Huet and R. Janečkovà, *J. Mol. Spectrosc.*, 2009, **254**, 55–68.

36 L. H. Coudert, W. Caminati, A. Maris and P. Ottaviani, *J. Mol. Spectrosc.*, 2010, **261**, 18–27.

37 J. T. Hougen, I. Kleiner and M. Godefroid, *J. Mol. Spectrosc.*, 1994, **163**, 559–586.

38 M. R. Aliev and J. T. Hougen, *J. Mol. Spectrosc.*, 1984, **106**, 110–123.

39 G. W. Robinson and C. D. Cornwell, *J. Chem. Phys.*, 1953, **21**, 1436–1442.

40 S. Kassi, D. Petitprez and G. Wlodarczak, *J. Mol. Struct.*, 2000, **517-518**, 375 – 386.

41 M. Tudorie, L. H. Coudert, T. R. Huet, D. Jegouso and G. Sedes, *J. Chem. Phys.*, 2011, **134**, 074314.

42 S. Kassi, D. Petitprez and G. Wlodarczak, *J. Mol. Spectrosc.*, 2004, **228**, 293–297.

43 P. A. Pella, *J. Chem. Thermodyn.*, 1977, **9**, 301–305.

44 H. M. Pickett, *J. Mol. Struct.*, 1991, **148**, 371–377.

45 B. J. Drouin, *J. Mol. Struct.*, 2017, **340**, 1–15.

46 R. Krishnan, J. S. Binkley, R. Seeger and J. A. Pople, *J. Chem. Phys.*, 1980, **72**, 650–654.

47 A. McLean and G. Chandler, *J. Chem. Phys.*, 1980, **72**, 5639–5648.

48 J.-D. Chai and M. Head-Gordon, *Phys. Chem. Chem. Phys.*, 2008, **10**, 6615–6620.

49 *Spartan 20*, http://www.wavefun.com.

50 M. L. Senent, S. Dalbouha, A. Cuisset and D. Sadovskii, *J. Phys. Chem. A*, 2015, **119**, 9644–9652.

51 G. C. Hancock, P. Rejto, R. Steckler, F. B. Brown, D. W. Schwenke and D. G. Truhlar, *J. Chem. Phys.*, 1986, **85**, 4997–5003.

52 F. Hindle, R. Bocquet, A. Pienkina, A. Cuisset and G. Mouret, *Optica*, 2019, **6**, 1449.

53 C. Elmaleh, F. Simon, J. Decker, J. Dumont, F. Cazier, M. Fourmentin, R. Bocquet, A. Cuisset, G. Mouret and F. Hindle, *Talanta*, 2022, 124097.